Remote Sensing in Ecology and Conservation
Open Access
ZSL

RESEARCH ARTICLE

Unoccupied aerial vehicles as a tool to map lizard operative temperature in tropical environments

Emma A. Higgins[1,2], Doreen S. Boyd[1], Tom W. Brown[3], Sarah C. Owen[1], Geertje M. F. van der Heijden[1] & Adam C. Algar[4]

[1]School of Geography, University of Nottingham, Nottingham NG7 2RD, United Kingdom
[2]Department of Biological and Forensic Sciences, University of South Wales, Pontypridd CF37 4BB, United Kingdom
[3]Kanahau Utila Research and Conservation Facility, Isla de Utila, Islas de Bahia, Honduras
[4]Department of Biology, Lakehead University, Thunder Bay, Ontario P7B 5E1, Canada

Keywords
Climate change, ectotherms, forest canopy, random forest, thermal suitability, UAVs

Correspondence
Doreen S. Boyd, School of Geography, University of Nottingham, Nottingham NG7 2RD, United Kingdom.
Email: doreen.boyd@nottingham.ac.uk

Funding Information
This work was funded by the University of Nottingham's Life in Changing Environments Research Priority Area and a School of Geography PhD studentship to EAH.

Editor: Temuulen Sankey
Associate Editor: Larissa Sayuri Moreira Sugai

Received: 18 July 2023; Revised: 28 February 2024; Accepted: 19 March 2024

doi: 10.1002/rse2.393

Abstract

To understand how ectotherms will respond to warming temperatures, we require information on thermal habitat quality at spatial resolutions and extents relevant to the organism. Measuring thermal habitat quality is either limited to small spatial extents, such as with ground-based 3D operative temperature (T_e) replicas, representing the temperature of the animal at equilibrium with its environment, or is based on microclimate derived from physical models that use land cover variables and downscale coarse climate data. We draw on aspects of both these approaches and test the ability of unoccupied aerial vehicle (UAV) data (optical RGB) to predict fine-scale heterogeneity in sub-canopy lizard (*Anolis bicaorum*) T_e in tropical forest using random forest models. *Anolis bicaorum* is an endemic, critically endangered, species, facing significant threats of habitat loss and degradation, and work was conducted as part of a larger project. Our findings indicate that a model incorporating solely air temperature, measured at the centre of the 20 × 20 m plot, and ground-based leaf area index (LAI) measurements, measured at directly above the 3D replica, predicted T_e well. However, a model with air temperature and UAV-derived canopy metrics performed slightly better with the added advantage of enabling the mapping of T_e with continuous spatial extent at high spatial resolutions, across the whole of the UAV orthomosaic, allowing us to capture and map T_e across the whole of the survey plot, rather than purely at 3D replica locations. Our work provides a feasible workflow to map sub-canopy lizard T_e in tropical environments at spatial scales relevant to the organism, and across continuous areas. This can be applied to other species and can represent species within the same community that have evolved a similar thermal niche. Such methods will be imperative in risk modelling of such species to anthropogenic land cover and climate change.

Introduction

Thermal habitat quality, i.e. favourable microclimatic conditions, is an important factor for ectothermic organisms (Higgins et al., 2021). The thermal environment impacts both performance and distribution of ectotherms by influencing metabolic and ecological function, as well as evolutionary fitness, through the interaction between physiology, behaviour, biophysics and microclimate (Campbell & Norman, 1998; Gates, 1980; Huey & Slatkin, 1976). This can scale to influence population dynamics (Diaz, 1997; Sinervo et al., 2010). Although temperature influences all levels of biological organization (Niehaus et al., 2012), the spatial resolution at which thermal environments have usually been measured is often far too coarse to be relevant to the thermal landscape experienced by individual organisms (Logan et al., 2013; Sears et al., 2011; Sears & Angilletta, 2015).

Quantifying fine-scale thermal environments for ectothermic organisms has traditionally taken two approaches: microclimate–biophysical modelling and field-based measures using thermal replicas. The former generally relies on mechanistic models that downscale broad-scale (usually monthly) macro-climate (≥1 km grid) data to estimate microclimate in specific habitats, e.g. NicheMapR, Microclima and Microclimc (Kearney & Porter, 2017; Maclean et al., 2018; Maclean & Klinges, 2021). These estimates of microclimate must then be combined with biophysical heat exchange models to estimate animal operative temperature (T_e), the temperature of the animal at equilibrium with its environment (Bakken, 1992; Logan et al., 2013), e.g. the ectotherm model in NicheMapR (Kearney & Porter, 2020). These models have revolutionized our ability to model thermal environments across broad spatial extents, especially for species distribution modelling, and new developments have the potential to model much finer variation (e.g. Microclimc), but applications at scales of individual organismal movement (e.g. cms to m) are still rare.

Alternatively, measuring the thermal environment and thermal habitat quality at spatial resolutions relevant to individual animals is standard practice for thermal ecologists using ground-based methods. This includes measuring T_e by deploying morphologically accurate 3D replicas of the focal species, fitted with temperature data loggers, in different microhabitats (Bakken, 1989; Logan et al., 2013; Muñoz & Losos, 2017). This allows the T_e of the focal species to be measured in different microhabitats at very fine spatial resolutions. However, each replica provides a point measure, sampling only a very small extent of thermal habitat and thus may not represent the conditions mere metres away. This can be partially resolved by using additional replicas, but this quickly increases, beyond feasibility, the cost and resources required for such methods, including replica materials, data loggers and deployment effort. These limitations of existing methods are particularly pertinent given the established importance of spatial heterogeneity of thermal environment for species, particularly ectotherms (Huey, 1974; Sears et al., 2016; Sears & Angilletta, 2015).

Continuous mapping of animal operative temperatures at fine scales relevant to those perceived by organisms has considerable potential to increase our understanding of thermal ecology, including how environmental change alters thermal environments and the implications of these changes for species occurrence, population persistence and ecological interactions. For example, spatial structure and heterogeneity, i.e. patchiness, of thermal environments, along with the mean temperature, influences thermoregulatory performance and movement of ectotherms, with considerable effects on energy expenditure (Sears & Angilletta, 2015). Combining fine-scale maps of operative temperature with organisms' thermal performance curves can be used to estimate thermal habitat quality and provide insights into the vulnerability, or robustness, of species to warming environments (Logan et al., 2013, 2015; Sinclair et al., 2016).

Remote sensing can improve the spatial resolution of mechanistic microclimate model outputs by capturing fine-scale measures of important data inputs such as topography and canopy metrics (Duffy et al., 2021; Milling et al., 2018; Zellweger et al., 2019). Canopy cover influences the thermal environment in multiple ways, including reducing incoming solar radiation (Campbell & Norman, 1998). In forests, the canopy acts as a thermal insulator, keeping the understory cool when ambient temperatures are hot, and keeping the understory warm when ambient temperatures are cold (De Frenne et al., 2019). Canopy features, such as Leaf Area Index (LAI), which is the one-sided area of leaves per unit ground area and is a measure of canopy density, have been found to influence operative and body temperatures of ectotherms, specifically lizards (Algar et al., 2018; Kearney et al., 2009), as well as spatial variation in lizard population abundance via effects on thermal environment (Higgins et al., 2021). These relationships suggest that, in wooded environments, fine-scale variation in canopy density and structure can be exploited to quantify the thermal heterogeneity available to individual organisms. Remote sensing technologies, such as unoccupied aerial vehicles (UAVs), can aid in capturing this canopy variation via optical sensors (most commonly RGB) and photogrammetry methods such as Structure from Motion (SfM) (Duffy et al., 2021; Milling et al., 2018; Zellweger et al., 2019). Although capturing specific canopy measures such as LAI from UAVs is challenging (Duffy et al., 2021), other measures of vegetation structure, such as greenness indices (Morris et al., 2013) and texture metrics, can be used as proxies for canopy cover and heterogeneity and are more straightforward to capture.

Here, we combine remote sensing and thermal ecology field methods to predict centimetre-scale variation in T_e of the endemic lizard *Anolis bicaorum* below the canopy, across the spatial extent of an entire UAV orthomosaic, covering the entirety of the 20 × 20 m survey plot. *Anolis bicaorum* is an endemic, critically endangered species, facing threats relevant to its thermal habitat (habitat loss, tropical forest degradation) that was being studied as part of a larger research project, where we are aware of its thermal habitat requirements (Higgins et al., 2021; Logan et al., 2013). We integrate 3D replicas, air temperature and high-resolution RGB imagery captured from a UAV across a series of plots on the island of Utila, Honduras, to predict fine-scale, continuous variation in T_e. We

compare model performance to models using ground-based LAI measures taken using a ceptometer and then demonstrate how we can predict T_e across UAV images for later use in mapping thermal habitat quality.

Materials and Methods

Study area and species

We carried out fieldwork on the island of Utila, Honduras (16.0950° N, 86.9274° W). The island is relatively homogenous in elevation, with a single notable elevation, Pumpkin Hill which reaches 74 m above sea level (Fig. S1). We surveyed sixteen 20 × 20 m plots that varied in their level of human disturbance, from relatively intact neotropical dry forest (no. of plots = 8), urban/degraded forest areas (no. of plots = 4), to heavily disturbed, sparsely treed areas in Utila Town (no. of plots = 4). For further information on plots, including locations, please see (Fig. S2; Table S1). The work was conducted between March and June of 2019, in the dry season of Utila, Honduras, where temperatures are on average around 29–31°C. The island experiences its rainy season between October and February, where temperatures are on average slightly lower at around 28°C and there is a higher incidence of rainfall.

Anolis bicaorum, the focus species of this work, was first described by Köhler (1996). *A. bicaorum* is endemic to the island of Utila, Honduras, and is found predominantly in forests (Brown et al., 2017) and its thermal ecology reflects these relatively cool, thermally homogeneous environments (Logan et al., 2013). Its preferred temperature range (T_{pref}) is 25.5 ± 1.29°C to 28.0 ± 1.27°C (Higgins et al., 2021), and its critical thermal maximum (CT_{max}) is 33.2°C (Logan et al., 2013). It faces significant threats from habitat loss and habitat degradation from development on the island of Utila (personal observation).

Ground measures

We measured T_e of different microhabitats in each plot using 20 morphologically accurate 3D replicas of *A. bicaorum* fitted with iButton dataloggers, as in Higgins et al. (2021). Replica position within the plot, substrate (trunk vs. ground), height (0–250 cm in 15-cm increments) and compass orientation (0–360° in 45° increments) were randomly chosen using a random number generator, as in Higgins et al. (2021). Replicas were placed randomly within the plot and all replica locations were recorded with a Spectra Pro Mark 120 differential DGPS. Mean horizontal recording error of the DGPS was 0.86 cm. The iButtons recorded T_e every 15 min. To determine the influence of the canopy structure directly above the replica on incoming solar radiation, we extracted T_e at solar noon on each day for subsequent modelling. Hourly plot air temperature (T_a) was recorded at a height of 1.5 m using a shaded DS1921G-F5 iButton as close to the centre of each plot as possible. The T_a of each plot at solar noon was extracted for each day the replicas were *in situ*. For detail on solar noon data extraction please see Supporting Information.

We measured leaf area index (LAI) above each of the 3D replicas at solar noon using an Accupar LP80 ceptometer, with a spatial resolution of 1 m. LAI was calculated using a simplified version of the Norman-Jarvis model (1975) See Supporting Information for details.

Unoccupied aerial vehicle (UAV) imagery

Ultra-high spatial resolution aerial imagery of each plot was acquired using a DJI Phantom 4 Advanced quadcopter UAV equipped with an integrated RGB (red, blue, green), 1-inch, 20-megapixel CMOS sensor mounted on a three-axis, gyro-stabilized gimbal. The UAV has an integrated GPS and GLONASS positioning system. The flights were conducted during calm conditions to avoid wind effects on leaves (Waite et al., 2019). A flight altitude of between 40 and 50 m was required to fly at a height of ×1.5 the height of the canopy, a full list of flight altitudes per plot can be seen in Supporting Information. All flights captured data at a 90 by 90% forward and side image overlap, affording orthomosaics of the canopies in each plot. UAV images were processed in Agisoft Metashape Professional V1.6.6, to create a 3-band RGB orthomosaic image for each plot, projected to WGS1984 UTM zone 16N. Resultant orthomosaics had a mean pixel spatial resolution of 0.9 cm per pixel and validated for spatial accuracy by visually comparing known points (buildings, roads etc.) to base maps and also DGPS points taken in the field at each plot. No shifting of the coordinates was necessary.

Imagery canopy metrics

As a proxy for canopy presence and density, the proportion of green (greenness) of each pixel within the orthomosaic was calculated using Equation (1) (Morris et al., 2013). An example output can be found in Supporting Information.

$$\text{Greenness} = \frac{\text{Green}}{(\text{Red} + \text{Green} + \text{Blue})} \quad (1)$$

To capture measures of canopy heterogeneity and structure, texture analyses were carried out on the greenness output. Grey-level co-occurrence matrix texture

analysis was undertaken using the *glcm* package in R version 4.1.0, using a 3×3 moving window to produce the following texture metrics: Homogeneity, Contrast, Dissimilarity, Entropy, Mean, Second-Moment and Variance. Example output can be seen in Figure S3.

Extracting UAV canopy metrics

We extracted values for the 8 canopy measures (7 texture layers and 1 greenness layer) above each 3D lizard replica using a 1 m buffer. This ensured capture of canopy variation across a sufficient spatial area given spatial accuracy, rather than based on a single 0.9 cm pixel. The mean pixel values for each layer within the buffer area around the 3D replica locations were extracted using the raster package in R version 4.1.0 (Hijmans, 2022).

Statistical analyses

We fitted regression random forest (RF) models using the ModelMap (Freeman & Frescino, 2009) package (Fig. 1). Random forest algorithms are particularly useful in working with linear and non-linear relationships within the same model; they also provide estimates of variable importance (Breiman, 2001). We randomly divided the data into a training (75%) and test set (25%) for independent model validation. We fitted four RF models to the T_e data. The first included plot T_a and ground-based LAI measures as predictors, the second included only UAV-based canopy measures, the third included UAV-based canopy measures and plot T_a, and the fourth incorporated all variables (ground-based LAI, plot T_a, and UAV canopy measures). All RF models were run with 500 trees, as varying tree number made little difference to model outcomes; for full details and model parameters of RF models, see the Table S3.

To validate RF models, we used the model diagnostic function in ModelMap to compare observed and predicted T_e values for the test dataset. The function also provided variable importance plots based on mean decrease accuracy (%IncMSE), which expresses the accuracy lost by the model when each variable is excluded; the higher the value, the more important the variable is to the model. Random forest algorithms are generally insensitive to multicollinearity of variables (Tang et al., 2020), but it can be a factor when trying to disentangle the influence of two correlated variables. Although our texture variables were correlated (See Supporting Information), we did not attempt to disentangle specific variables of importance between the texture variables, so our interpretation will be robust to this multicollinearity.

To evaluate predictive performance across different survey plots, we used a Jackknife approach where one plot was omitted from the RF training data and the data from the remainder of the plots were used to predict the omitted plot. This was then repeated omitting each plot separately and refitting the T_e.Air.UAV model.

To determine whether RF modelling with UAV data improved the ability to predict T_e compared to air temperature alone, we also fitted a regression of T_e against T_a. As simple biophysical models of T_e predict a linear relationship between T_a and T_e (Algar et al., 2018), we

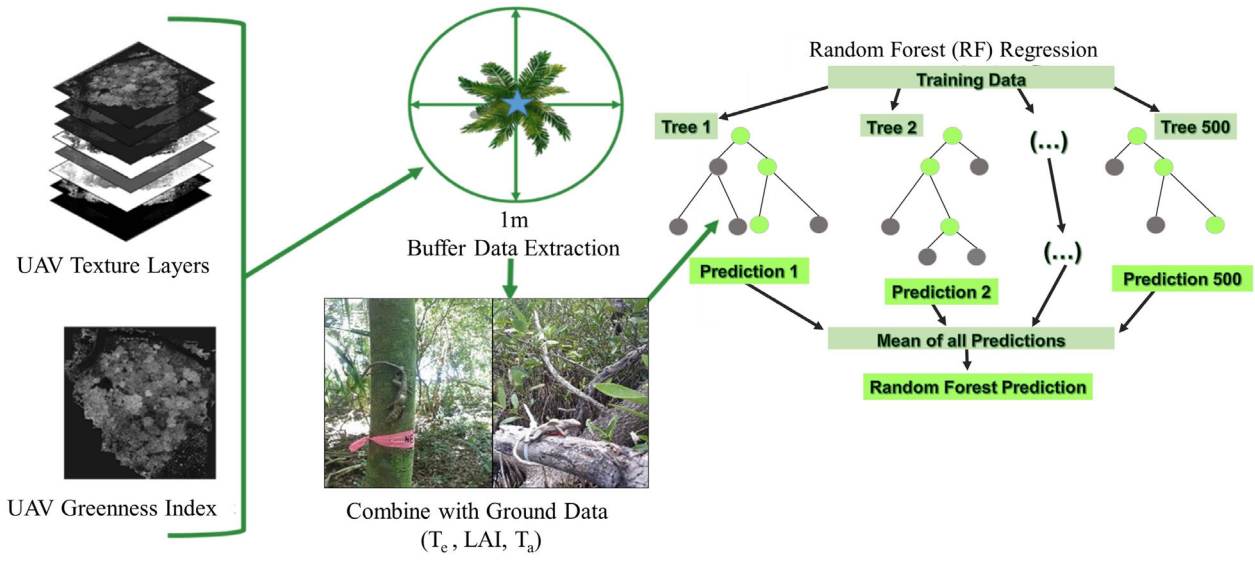

Figure 1. Simple workflow of data included in Random Forest Regression models.

first fitted a simple linear regression. However, as the T_e–T_a relationship exhibited potential curvilinearity, we also fitted a third-order polynomial relationship.

Mapping thermal habitat

To map T_e across the whole of each plot, we used the predict function in ModelMap to predict across the UAV orthomosaics. We assumed T_a was homogeneous across the plot. Mean T_a at solar noon across plots was 30.4°C. Therefore, using the conditional function in Raster Calculator in ArcMap 10.4.1, a uniform raster layer with the same spatial resolution and spatially matching pixel grid as the other input variables was used to represent T_a, at 30.4°C. The T_a was kept continuous between plots to demonstrate that users can compare suitability of different habitats at similar air temperatures and that the model can be run at any air temperature, which can be helpful to look at air temperature warming scenarios.

Results

Prediction of T_e

T_e increased with T_a and the linear regression was significant ($F = 1162$, d.f. = 793, $P = < 0.001$; adjusted $r^2 = 0.59$). However, the relationship showed considerable heteroscedasticity (Fig. 2), with greater variance at warmer temperatures. Fitting a third-order polynomial did not substantially improve model fit (Fig. 2; $F = 392.9$, d.f. = 791, $P = < 0.001$, adjusted $r^2 = 0.60$).

Results of the RF model incorporating ground-based data alone (Model = T_e.ground), indicated that using only plot level T_a and LAI within the model accounted for 73.2% of the variation in T_e. Model validation revealed a strong relationship between observed and predicted values (Fig. 3; adjusted $r^2 = 0.89$, $P = < 0.001$). The RF model using only UAV-derived data (Model = T_e.UAV) accounted for only 30.26% of the variation in T_e. Model validation revealed a negligible relationship between observed and predicted values in the test data (Fig. 3; adjusted $r^2 = 0.07$, $P = < 0.001$). However, including the influence of T_a in the random forest along with the UAV metrics (Model = T_e.Air.UAV) accounted for 82.82% of the variation in T_e. Model validation revealed a strong relationship between observed and predicted values (Fig. 3; adjusted $r^2 = 0.91$, $P = < 0.001$). The RF model, which included ground and UAV-based variables (Model = T_e.All), explained the most (85.99%) variation within T_e. Model validation revealed a strong relationship between observed and predicted values in the test data (Fig. 3; adjusted $r^2 = 0.91$, $P = < 0.001$). Variable importance plots for each of the models can be found in Figures S6 and S9.

The jackknifing approach to model evaluation showed that predictions vary substantially between plots and land

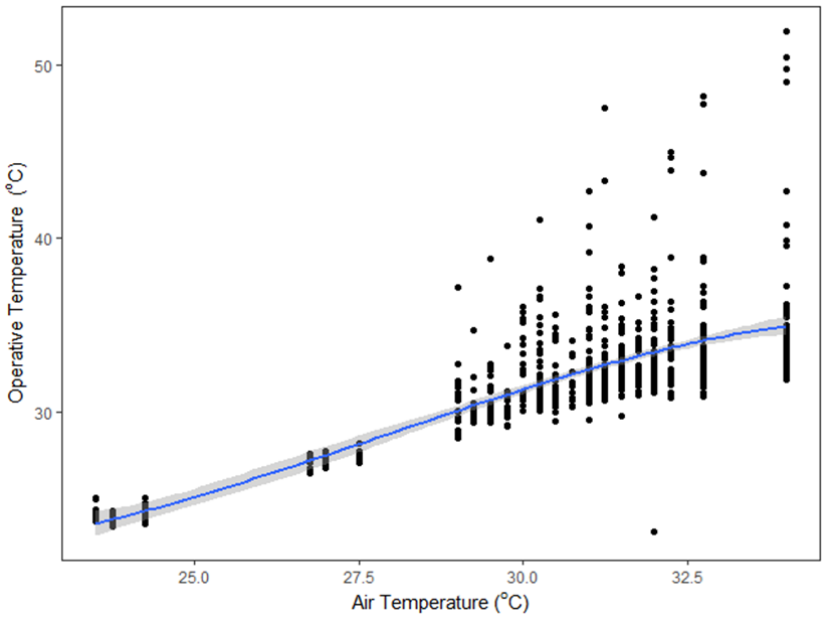

Figure 2. Air temperature versus T_e fitted with a third-order polynomial curve. Each point is the T_e (°C) at solar noon of a 3D replica within a plot, plotted against the air temperature (°C) within the plot at solar noon. Blue curved line indicates third-order polynomial curve and lighter shading around the curve = 95% confidence intervals.

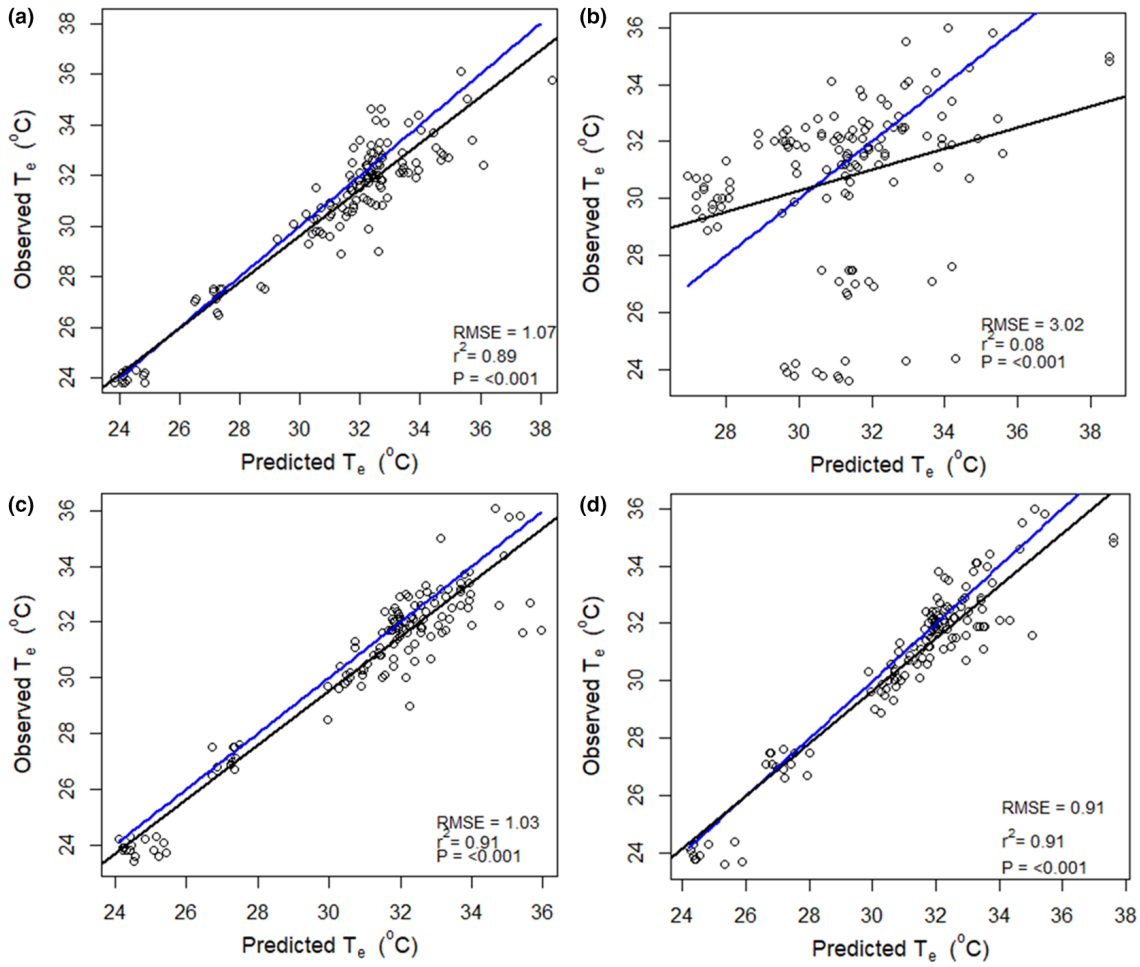

Figure 3. Scatterplot of observed T_e versus predicted T_e values for the test data for each random forest model. (A) T_e.Ground, (B) T_e.UAV, (C) T_e.Air.UAV, (D) T_e.All. RMSE, root mean square error, adjusted r^2 and associated P value derived from correlation of observed versus predicted T_e. Black line indicates linear regression line and the blue line indicates one-to-one line.

cover classes (Fig. 4). Forested plots generally had higher r^2 values between the observed and predicted values for T_e than those found for urban forest and urban plots with little vegetation. Figure 4 indicates a bimodal structure in the majority of forest plots. This is likely due to the cluster of cooler temperatures being where 3D replicas are in areas where there is a more closed and shaded canopy, resulting in more stable and lower temperatures, and the higher temperatures indicating where replicas were exposed to more solar radiation, likely in canopy gaps. The plot in Figure 4K is an exception to this bimodal structure. This plot was a coastal forest located on the beach at the south-eastern point of the island, with exposed winds. The canopy consisted solely of Caribbean almond (*Terminalia catappa*) trees which form a unique forest structure with no understory present. Canopy make-up, coastal winds and proximity to volcanic rock exposures all may have influenced the thermal regime of this plot, and the ability for the RF model to predict temperatures within this plot, as the model is based solely on canopy structure. However, the plots in Figure 4B and C were also coastal almond forest and still showed the bimodal structure of other forested plots. Further figures outlining model performance by land cover, looking specifically at performance by temperature grouping, can be seen in the Supporting Information.

Mapping T_e

We used the model T_e.Air.UAV, which included T_a and the UAV metrics (greenness and textures), to map T_e across the whole of each plot. Figures 5 and 6 show example raster layers for areas surrounding survey plots including the original RGB imagery and the T_e prediction

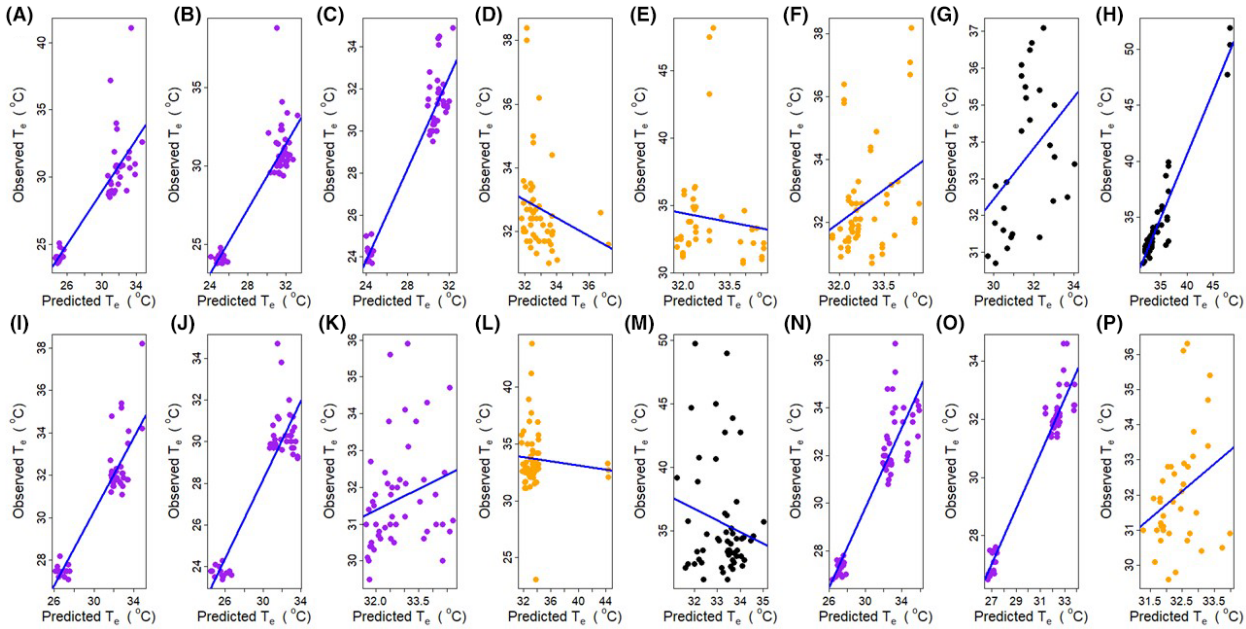

Figure 4. Observed versus predicted T_e for each plot using the T_e.Air.UAV random forest model with a Jackknifing approach. Labels (A) to (P) correspond to Plot number sequentially from 1 to 16. Point colours refer to land cover where purple = forested plots, orange = urban forest plots and black = urban plots. Blue lines indicate a line of best fit.

raster based on the T_e.Air.UAV RF model. Figures 5 and 6 show RGB and T_e raster maps for a subset of forest and an urban area; similar figures for the remainder of the plots can be seen in the Supporting Information. Maps highlight the whole of the orthomosaic as well as regions of interest to evaluate mapping performance. In forests (e.g. Fig. 5), the model identifies large T_e differences associated with closed canopies but also more subtle differences between tree species, with some species having more open canopies that allow more solar radiation to reach sub-canopy dwelling ectotherms. Examining plots within urban areas (e.g. Fig. 6), the model has picked up gaps and closed canopy areas, but there are some small discrepancies in relation to water and buildings (rooftops). This corroborates results of the Jackknife approach for the model (Fig. 4; Table S4), which showed that the model performed better in forested areas.

Discussion

Canopy structure, measured using UAV RGB imagery, has the potential to provide fine-scale predictions of

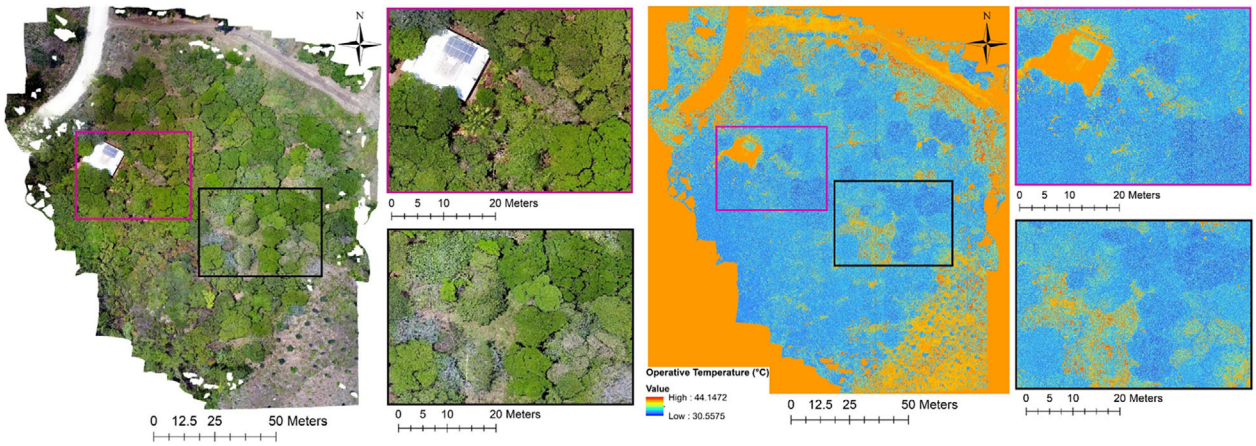

Figure 5. Left Images = True Colour (RGB) raster layer of area surrounding Plot 1. Right Images = Operative Temperature (T_e) raster layer derived from predictions of T_e.Air.UAV random forest model of area surrounding Plot 1. Magenta and black insets highlight areas of interest.

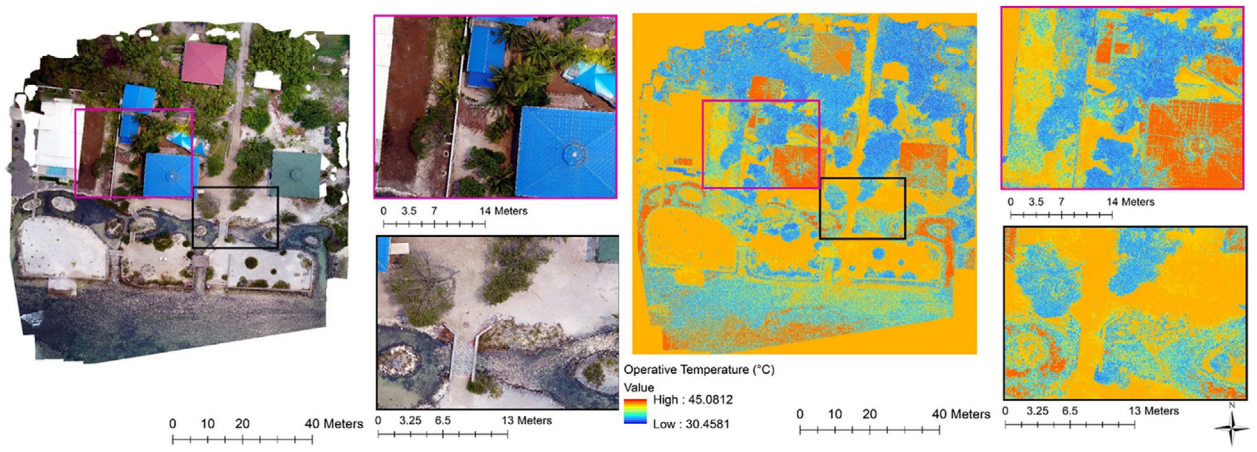

Figure 6. Left Images = True Colour (RGB) raster layer of area surrounding Plot 7. Right Images = Operative Temperature (T_e) raster layer derived from predictions of T_e.Air.UAV random forest model of area surrounding Plot 7. Magenta and black insets highlight areas of interest.

spatial heterogeneity of thermal habitat quality for animals at finer resolution than can currently be obtained from existing mechanistic models, or from ground-based methods traditionally used in thermal ecology. Here we have proposed a workflow for mapping sub-canopy tropical lizard T_e at fine spatial resolutions using high-resolution optical UAV imagery coupled with T_a data. This proposed workflow allows for high spatial resolution and spatial extent measures of T_e below the canopy and can be easily extended to other taxa, helping fulfil the need for data on T_e for forest-dwelling ectothermic organisms at ecologically relevant spatial resolutions and extents.

Results of the RF regression models indicated that the model including T_a and the combined UAV data (greenness and texture) had higher predictive performance of T_e than models using just T_a or coupling T_a with ground-based LAI measurements. T_a accounted for the most variation in T_e, as a lone variable. In the models where it was included, it always was the most important variable within the model, as expected from biophysical theory (Campbell & Norman, 1998; Gates, 1980; Sears et al., 2011). Determining whether estimates from T_a from microclimate models can perform as well as T_a measures taken *in situ* is an obvious next research step. As we predicted, adding a ground-based measure of LAI into these models increased model performance, again consistent with theoretical expectations (Maclean & Klinges, 2021) and empirical findings from broader scales (Algar et al., 2018). However, we also found that including UAV-derived canopy measurements in the model with air temperature accounted for a higher percentage of variation within T_e than using air temperature and ground-based LAI. This suggests that greenness and texture captured biophysically relevant aspects of the canopy that influence incident solar radiation beyond that captured by LAI measurements from the ground. Nonetheless, ground-based LAI, as only one variable, does well in the model when coupled with plot T_a. However, UAV-derived data also have the advantage of allowing T_e to be mapped across a larger spatial extent at higher spatial resolutions, with relatively simple data acquisition methods, which is not possible with ground-based LAI measures.

The T_e.Air.UAV model performed best within forested areas and less well in other land covers, including highly urban plots. For example, roofs of some urban buildings were also classified as cooler areas. Such failures are to be expected since; in such cases, the UAV imagery is capturing variation in the ground surface, rather than the influence of shade. This highlights the need to train the model further across different land covers, and, in the case of urban areas, considers that the modelling approach may not be suitable due to a general lack of canopy. In forests, where the model performed best, the findings are consistent with those of Algar et al., (Algar et al., 2018), who found that LAI improved microclimate-only models of lizard body temperature in closed canopy environments but had little influence in environments that were more open. Our findings demonstrate that these relationships hold across multiple orders of magnitude of spatial resolutions and extent ($1\,km^2$ and global extent in Algar et al. (2018) versus $<1\,m^2$ and $20\,m \times 20\,m$ plot extent here). The model is useful to thermal biologist and ecologists who can set out 20 thermal models in a plot and subsequently use the method proposed here to get a continuous prediction of T_e, across the survey area, rather than solely point-based measures from replica location,

allowing us to now calculate thermally suitable habitat area and to determine heterogeneity of thermal landscapes, which is relevant to species fitness and energetics (Sears et al., 2011; Sears & Angilletta, 2015).

UAVs are a promising method for capturing high-resolution spatial data for microclimate modelling (Duffy et al., 2021; Kašpar et al., 2021; Milling et al., 2018; Zellweger et al., 2019). This is, in large part, because canopy structure, which can be captured with UAVs, can produce significant differences in microclimate (Kašpar et al., 2021; Maclean & Klinges, 2021). UAVs themselves are becoming more accessible; however, they themselves can be costly, with certain sensors adding to the overall cost. However, this work was conducted using a standard RGB drone, and there are open-source cloud-based options for processing available. Detail on overall cost of method equipment and alternative cost options have been provided in Table S5. Our work extends previous work developing UAV-based approaches to spatially model microclimate (Duffy et al., 2021; Kaš par et al., 2021; Milling et al., 2018; Zellweger et al., 2019), to now map an ecologically relevant temperature measures (T_e), for ectotherms. Such maps will be valuable in testing hypotheses about individual organism thermoregulation, space use and energetics in response to the spatial structure of thermal habitat (Sears et al., 2011; Sears & Angilletta, 2015) thermal quality and to identify components of thermal habitat that influence population dynamics (Higgins et al., 2021). While here we only estimated thermal quality at solar noon, further work could extend our methods to capture fine-scale (e.g. hourly) variation in thermal quality at daily, weekly or seasonal temporal extents. Such information on thermally (un) favourable conditions would provide valuable insight into constraints on organismal time budgets which influence distribution, abundance and fitness (Caetano et al., 2020; Higgins et al., 2021; Logan et al., 2013, 2015). The ability to model T_e, even at a single point in time but across a complete landscape, including fine-scale heterogeneity, is step forward in measuring thermal habitat quality for ectotherms.

For the study species (*Anolis bicaourm*), this work has allowed us to capture plot-based thermal habitat measures at relevant spatial resolutions for the first time. The model performs well in forest environments, where *A. bicaorum* is predominantly found, and predicts the ranges within T_{pref} (25.5 ± 1.29°C to 28.0 ± 1.27°C) well. The model does underestimate the temperature at the higher ranges, which should be noted when looking at measures such as CT_{Max} for the species, which is 33.2°C. Therefore, future work will also look to improve model performance at higher temperatures in tropical forests. The model does however allow us to now calculate suitable thermal habitat at a better spatial resolution, rather than solely at a mean 20×20 m plot level. And now allows us to look at the suitability of the plot based on thermal heterogeneity and spatial arrangement of thermal patches, rather than solely on mean operative temperature measures, as was done by Higgins et al., 2021. This is major step forward when looking at quantifying thermal habitat for such species under threat and can help us look at the impacts of habitat degradation, such as selective logging, on the thermal environment, and help us predict species responses to anthropogenic land use and climate change.

Future work toward improving model predictions could incorporate additional UAV data, such as canopy volumetric data from structure from motion (SfM) photogrammetry (Duffy et al., 2021; Zellweger et al., 2019). In addition, UAV-derived tree and canopy height, which are also significantly related to microclimate (Kašpar et al., 2021), could also improve models. Such additional measures are relatively simple to obtain methodologically from UAV-derived data. Future work will also look to test this approach with different species of interest and during different seasons, to test the model's performance in different weather conditions. Other recommendations for future research would be to test the model across different geographic areas. For example, the neighbouring island of Roatan has dramatically different topographical features; therefore, the model could theoretically be tested there to determine its validity across different more topographically complex landscapes. Another avenue of research would be to test the workflows and models proposed against well-established mechanistic models such as NichemapR and Microclimc or even to combine the two approaches, gathering additional data from mechanistic microclimate modelling to add to the model proposed here. Some research has been conducted on differences in performance of mechanistic and empirical models, e.g. Kearney et al. (2014), where both modelling avenues were found to perform similarly, but with different limitations. Future research on this topic would greatly benefit how we use such models to map species responses to climate and land use change.

Our work has provided a step forward in mapping ectotherm T_e at fine spatial resolution using optical UAV data coupled with T_a. This workflow and model will allow us to map ecologically relevant measures of the thermal environment across larger areas at scales relevant to the individual animals and populations, something that until now was not feasible with standard ground-based methods or with mechanistic niche modelling. This opens new avenues to understanding the impact of anthropogenic and climate change on species, especially in forests, that are dependent on suitable thermal environments, like *A. bicaorum*.

Acknowledgments

We thank Kanahau Utila Research and Conservation Facility (KURCF), Honduras for supporting fieldwork, to all the KRCF staff (Flavia Diotallevi, Andrea Martinez, Daisy Maryon, Bryan Rüsell Neper Escalante & Ana Daniella Sansur) and to all of the field assistants that aided with the data collection. We also thank J. Streicher and the Natural History Museum, London, for access to anole specimens for 3D scanning.

References

Algar, A.C., Morley, K. & Boyd, D.S. (2018) Remote sensing restores predictability of ectotherm body temperature in the world's forests. *Global Ecology and Biogeography*, **27**, 1412–1425. Available from: https://doi.org/10.1111/geb.12811

Bakken, G.S. (1989) Arboreal perch properties and the operative temperature experienced by small animals. *Ecology*, **70**, 922–930. Available from: https://doi.org/10.2307/1941359

Bakken, G.S. (1992) Measurement and application of operative and standard operative temperatures in ecology. *American Zoologist*, **32**, 194–216. Available from: https://doi.org/10.1093/icb/32.2.194

Breiman, L. (2001). Random forests. *Machine Learning*, **45**, 5–32. https://doi.org/10.1023/A:1010933404324

Brown, T., Maryon, D., Vanderburg, T. & Lonsdale, G. (2017) Distribution and natural history notes on Norops bicaorum (Squamata: Dactyloidae) endemic to Isla de Utila, Hondruas. *Mesoamerican Herpetology*, **4**(2), 493–497.

Caetano, G.H.O., Santos, J.C., Godinho, L.B., Cavalcante, V.H.G.L., Diele-Viegas, L.M., Campelo, P.H. et al. (2020) Time of activity is a better predictor of the distribution of a tropical lizard than pure environmental temperatures. *Oikos*, **129**, 953–963. Available from: https://doi.org/10.1111/oik.07123

Campbell, G.S. & Norman, J.M. (1998) *An introduction to environmental biophysics*, 2nd edition. New York: Springer-Verlag.

De Frenne, P., Zellweger, F., Rodríguez-Sánchez, F., Scheffers, B.R., Hylander, K., Luoto, M. et al. (2019) Global buffering of temperatures under forest canopies. *Nature Ecology & Evolution*, **3**, 744–749. Available from: https://doi.org/10.1038/s41559-019-0842-1

Diaz, J.A. (1997) Ecological correlates of the thermal quality of an ectotherm's habitat: a comparison between two temperate lizard populations. *Functional Ecology*, **11**, 79–89. Available from: https://doi.org/10.1046/j.1365-2435.1997.00058.x

Duffy, J.P., Anderson, K., Fawcett, D., Curtis, R.J. & Maclean, I.M.D. (2021) Drones provide spatial and volumetric data to deliver new insights into microclimate modelling. *Landscape Ecology*, **36**, 685–702. Available from: https://doi.org/10.1007/s10980-020-01180-9

Freeman, E. & Frescino, T. (2009) *ModelMap: modeling and map production using random Forest and stochastic gradient boosting*. Ogden, UT, USA: USDA Forest Service, Rocky Mountain Research Station.

Gates. (1980) *Biophysical ecology*. New York: Springer-Verlag.

Higgins, E.A., Boyd, D.S., Brown, T.W., Owen, S.C. & Algar, A.C. (2021) Disentangling controls on animal abundance: prey availability, thermal habitat, and microhabitat structure. *Ecology and Evolution*, **11**, 11414–11424. Available from: https://doi.org/10.1002/ece3.7930

Hijmans, R.J. (2022) raster: Geographic Data Analysis and Modeling. R package version 3.5–15. https://CRAN.R-project.org/package=raster

Huey, R.B. (1974) Behavioral thermoregulation in lizards: importance of associated costs. *Science*, **184**, 1001–1003.

Huey, R.B. & Slatkin, M. (1976) Cost and benefits of lizard thermoregulation. *The Quarterly Review of Biology*, **51**, 363–384. Available from: https://doi.org/10.1086/409470

Kašpar, V., Hederová, L., Macek, M., Müllerová, J., Prošek, J., Surový, P. et al. (2021) Temperature buffering in temperate forests: comparing microclimate models based on ground measurements with active and passive remote sensing. *Remote Sensing of Environment*, **263**, 112522. Available from: https://doi.org/10.1016/j.rse.2021.112522

Kearney, M., Shine, R. & Porter, W.P. (2009) The potential for behavioral thermoregulation to buffer "cold-blooded" animals against climate warming. *Proceedings of the National Academy of Sciences of the United States of America*, **106**, 3835–3840. Available from: https://doi.org/10.1073/pnas.0808913106

Kearney, M.R., Shamakhy, A., Tingley, R., Karoly, D.J., Hoffmann, A.A., Briggs, P.R. et al. (2014). Microclimate modelling at macro scales: a test of a general microclimate model integrated with gridded continental-scale soil and weather data. *Methods in Ecology and Evolution*, **5**, 273–286. https://doi.org/10.1111/2041-210X.12148

Kearney, M.R. & Porter, W.P. (2017) NicheMapR—an R package for biophysical modelling: the microclimate model. *Ecography*, **40**, 664–674. Available from: https://doi.org/10.1111/ecog.02360

Kearney, M.R. & Porter, W.P. (2020) NicheMapR—an R package for biophysical modelling: the ectotherm and dynamic energy budget models. *Ecography*, **43**, 85–96.

Köhler, G. (1996). Additions to the known herpetofauna of the Isla de Utila (Islas de la Bahia, Honduras) with description of a new species of the genus Norops (Reptilia: Iguanidae). *Senck biol*, **76**, 19–28.

Logan, M.L., Fernandez, S.G. & Calsbeek, R. (2015) Abiotic constraints on the activity of tropical lizards. *Functional Ecology*, **29**, 694–700.

Logan, M.L., Huynh, R.K., Precious, R.A. & Calsbeek, R.G. (2013) The impact of climate change measured at relevant spatial scales: new hope for tropical lizards. *Global Change*

Biology, **19**, 3093–3102. Available from: https://doi.org/10.1111/gcb.12253

Maclean, I.M.D. & Klinges, D.H. (2021) Microclimc: a mechanistic model of above, below and within-canopy microclimate. *Ecological Modelling*, **451**, 109567. Available from: https://doi.org/10.1016/j.ecolmodel.2021.109567

Maclean, I.M.D., Mosedale, J.R. & Bennie, J.J. (2018) Microclima: an r package for modelling meso- and microclimate. *Methods in Ecology and Evolution*, **10**, 280–290. Available from: https://doi.org/10.1111/2041-210X.13093

Milling, C.R., Rachlow, J.L., Olsoy, P.J., Chappell, M.A., Johnson, T.R., Forbey, J.S. et al. (2018) Habitat structure modifies microclimate: an approach for mapping fine-scale thermal refuge. *Methods in Ecology and Evolution*, **9**, 1648–1657. Available from: https://doi.org/10.1111/2041-210X.13008

Morris, D., Boyd, D., Crowe, J., Johnson, C. & Smith, K. (2013) Exploring the potential for automatic extraction of vegetation phenological metrics from traffic webcams. *Remote Sensing*, **5**, 2200–2218. Available from: https://doi.org/10.3390/rs5052200

Muñoz, M.M. & Losos, J.B. (2017) Thermoregulatory behavior simultaneously promotes and forestalls evolution in a tropical lizard. *The American Naturalist*, **191**, E15–E26. Available from: https://doi.org/10.1086/694779

Niehaus, A.C., Angilletta, M.J., Sears, M.W., Franklin, C.E. & Wilson, R.S. (2012) Predicting the physiological performance of ectotherms in fluctuating thermal environments. *The Journal of Experimental Biology*, **215**, 694–701. Available from: https://doi.org/10.1242/jeb.058032

Sears, M.W. & Angilletta, M.J. (2015) Costs and benefits of thermoregulation revisited: both the heterogeneity and spatial structure of temperature drive energetic costs. *The American Naturalist*, **185**, E94–E102. Available from: https://doi.org/10.1086/680008

Sears, M.W., Angilletta, M.J., Schuler, M.S., Borchert, J., Dilliplane, K.F., Stegman, M. et al. (2016) Configuration of the thermal landscape determines thermoregulatory performance of ectotherms. *Proceedings of the National Academy of Sciences of the United States of America*, **113**, 10595–10600. Available from: https://doi.org/10.1073/pnas.1604824113

Sears, M.W., Raskin, E. & Angilletta, M.J. (2011) The world is not flat: defining relevant thermal landscapes in the context of climate change. *Integrative and Comparative Biology*, **51**, 666–675. Available from: https://doi.org/10.1093/icb/icr111

Sinclair, B.J., Marshall, K.E., Sewell, M.A., Levesque, D.L., Willett, C.S., Slotsbo, S. et al. (2016) Can we predict ectotherm responses to climate change using thermal performance curves and body temperatures? *Ecology Letters*, **19**, 1372–1385. Available from: https://doi.org/10.1111/ele.12686

Sinervo, B., Mendez-de-la-Cruz, F., Miles, D.B., Heulin, B., Bastiaans, E., Villagran-Santa Cruz, M. et al. (2010) Erosion of lizard diversity by climate change and altered thermal niches. *Science*, **328**, 894–899. Available from: https://doi.org/10.1126/science.1184695

Tang, Z., Mei, Z., Liu, W. & Xia, Y. (2020) Identification of the key factors affecting Chinese carbon intensity and their historical trends using random forest algorithm. *Journal of Geographical Sciences*, **30**, 743–756. Available from: https://doi.org/10.1007/s11442-020-1753-4

Waite, C.E., Heijden, G.M.F., Field, R. & Boyd, D.S. (2019) A view from above: unmanned aerial vehicles (UAV s) provide a new tool for assessing liana infestation in tropical forest canopies. *Journal of Applied Ecology*, **56**, 902–912. Available from: https://doi.org/10.1111/1365-2664.13318

Zellweger, F., Coomes, D., Lenoir, J., Depauw, L., Maes, S.L., Wulf, M. et al. (2019) Seasonal drivers of understorey temperature buffering in temperate deciduous forests across Europe. *Global Ecology and Biogeography*, **28**, 1774–1786. Available from: https://doi.org/10.1111/geb.12991

Supporting Information

Additional supporting information may be found online in the Supporting Information section at the end of the article.

Figure S1. Elevation map of Utila, Honduras using Shuttle Radar Topography Mission (SRTM) 1- arc second digital elevation model. Elevation in metres above sea level.
Figure S2. Plot locations, number refers to Plot ID number.
Figure S3. UAV RGB Orthomosaic (left), UAV Greenness raster following Equation 1 (right) where 1 = high greenness and 0 = low greenness values.
Figure S4. Example of all texture layers for area surrounding Plot 1, (A) Dissimilarity, (B) Contrast, (C) Variance, (D) Homogeneity, (E) Mean, (F) Second Moment and (G) Entropy.
Figure S5. Correlation plot for all variables used in models.
Figure S6. Variable importance plot derived from model validation function for model T_e.Ground.
Figure S7. Variable importance plot for model T_e.UAV.
Figure S8. Variable importance plot for model T_e.Air.UAV.
Figure S9. Variable importance plot derived from model validation function for model T_e.Air.UAV.
Figure S10. Frequency of difference between observed and predicted T_e (°C) grouped by temperature bracket to determine what temperatures the model (T_e.Air.UAV – Jacknife) is best at predicting for Forest environments (Land Cover).

Figure S11. Frequency of difference between observed and predicted T_e (°C) grouped by temperature bracket to determine what temperatures the mode (T_e.Air.UAV – Jacknife) l is best at predicting for Urban Forest environments (Land Cover).
Figure S12. Frequency of difference between observed and predicted T_e (°C) grouped by temperature bracket to determine what temperatures the model (T_e.Air.UAV – Jacknife) is best at predicting for Urban environments (Land Cover).
Figure S13. Frequency of difference between observed and predicted T_e (°C) for the T_e.Air.UAV Jacknife Model for all three Land Covers (Forest, Urban and Urban Forest).
Figure S14. RGB raster layer of area surrounding Plot 2 with zoomed in and highlighted areas of interest (magenta and black insets).
Figure S15. Operative temperature (T_e) raster layer derived from predictions of T_e.Air.UAV random forest model of area surrounding Plot 2 with zoomed in and highlighted areas of interest (magenta and black insets).
Figure S16. RGB raster layer of area surrounding Plot 3 with zoomed in and highlighted areas of interest (magenta and black insets).
Figure S17. Operative temperature (T_e) raster layer derived from predictions of T_e.Air.UAV random forest model of area surrounding Plot 3 with zoomed in and highlighted areas of interest (magenta and black insets).
Figure S18. RGB raster layer of area surrounding Plot 5 with zoomed in and highlighted areas of interest (magenta and black insets).
Figure S19. Operative temperature (*Te*) raster layer derived from predictions of T_e.Air.UAV random forest model of area surrounding Plot 5 with zoomed in and highlighted areas of interest (magenta and black insets).
Figure S20. RGB raster layer of area surrounding Plot 8 with zoomed in and highlighted areas of interest (magenta and black insets).
Figure S21. Operative temperature (T_e) raster layer derived from predictions of T_e.Air.UAV random forest model of area surrounding Plot 8 with zoomed in and highlighted areas of interest (magenta and black insets).
Figure S22. RGB raster layer of area surrounding Plots 9 and 10 with zoomed in and highlighted areas of interest (magenta and black insets).
Figure S23. Operative temperature (*Te*) raster layer derived from predictions of T_e.Air.UAV random forest model of area surrounding Plots 9 and 10 with zoomed in and highlighted areas of interest (magenta and black insets).
Figure S24. RGB raster layer of area surrounding Plot 11 with zoomed in and highlighted areas of interest (magenta and black insets).
Figure S25. Operative temperature (*Te*) raster layer derived from predictions of T_e.Air.UAV random forest model of area surrounding Plot 11 with zoomed in and highlighted areas of interest (magenta and black insets).
Figure S26. RGB raster layer of area surrounding Plot 12 with zoomed in and highlighted areas of interest (magenta and black insets).
Figure S27. Operative temperature (T_e) raster layer derived from predictions of T_e.Air.UAV random forest model of area surrounding Plot 12 with zoomed in and highlighted areas of interest (magenta and black insets).
Figure S28. RGB raster layer of area surrounding Plot 13 with zoomed in and highlighted areas of interest (magenta and black insets).
Figure S29. Operative temperature (T_e) raster layer derived from predictions of T_e.Air.UAV random forest model of area surrounding Plot 13 with zoomed in and highlighted areas of interest (magenta and black insets).
Figure S30. RGB raster layer of area surrounding Plot 14 with zoomed in and highlighted areas of interest (magenta and black insets).
Figure S31. Operative temperature (T_e) raster layer derived from predictions of T_e.Air.UAV random forest model of area surrounding Plot 14 with zoomed in and highlighted areas of interest (magenta and black insets).
Figure S32. RGB raster layer of area surrounding Plot 15 with zoomed in and highlighted areas of interest (magenta and black insets).
Figure S33. Operative temperature (T_e) raster layer derived from predictions of T_e.Air.UAV random forest model of area surrounding Plot 15 with zoomed in and highlighted areas of interest (magenta and black insets).
Figure S34. RGB raster layer of area surrounding Plot 16 with zoomed in and highlighted areas of interest (magenta and black insets).
Figure S35. Operative temperature (T_e) raster layer derived from predictions of T_e.Air.UAV random forest model of area surrounding Plot 16 with zoomed in and highlighted areas of interest (magenta and black insets).
Figure S36. RGB raster layer of area surrounding Plot 6 with zoomed in and highlighted areas of interest (magenta and black insets).
Figure S37. Operative temperature (T_e) raster layer derived from predictions of T_e.Air.UAV random forest model of area surrounding Plot 6 with zoomed in and highlighted areas of interest (magenta and black insets).
Figure S38. RGB raster layer of area surrounding Plot 4 with zoomed in and highlighted areas of interest (magenta and black insets).
Figure S39. Operative temperature (T_e) raster layer derived from predictions of T_e.Air.UAV random forest model of area surrounding Plot 4 with zoomed in and highlighted areas of interest (magenta and black inset).

Table S1. Plot Location and descriptions for survey plots on Utila, Isla de Bahia, Honduras.
Table S2. Flight altitude of the UAV flight for each plot.
Table S3. Details of all RF models conducted; Mtry = the number of variables randomly chosen at each split, Ntrees = number of trees grown within RF model.
Table S4. Random forest validation outcome for each plot using the T_e.Air.UAV random forest model with a Jackknifing approach, where the plot indicated in the Plot No. column was omitted from training data and then used as a validation set, r^2 and the associated *P*-value derived from correlation of observed versus predicted T_e.
Table S5. Comparison of method equipment and software costs and lower cost alternatives (where possible).